EXTENDED DATA; SUPPORTING INFORMATION

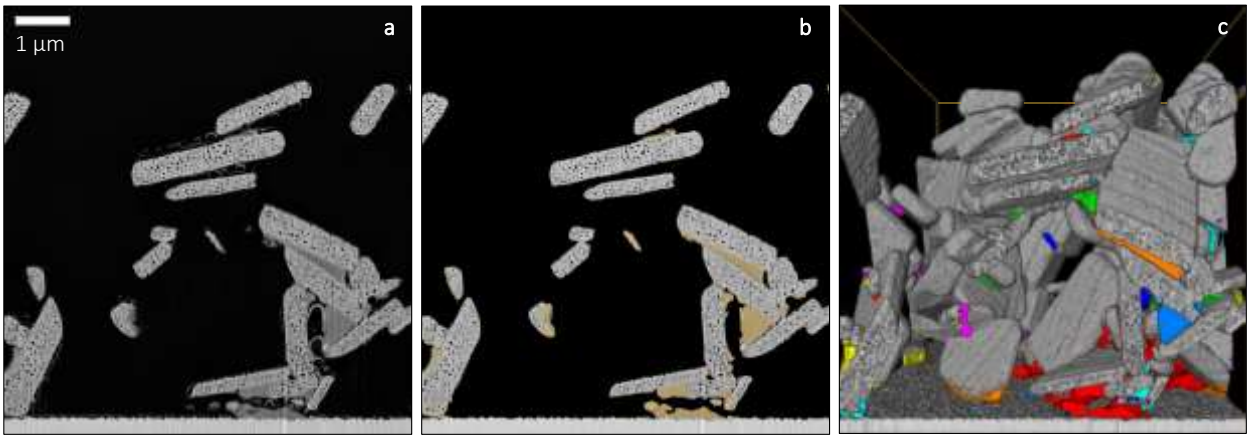

Figure S1: (a) Detailed view of a SEM cross-section (*xz*-plane) in *sample (ii)*, the LTON photoelectrode. The air bubbles in the epoxy were formed during the embedding process and removed from the images by a low pass filter. (b) The golden false colored areas are the TiO_2 necking phase and were segmented by a machine-learning algorithm [14] trained on manual selections of the uniform grey areas (TiO_2 necking phases). (c) 3D rendering of the LTON photoelectrode with the TiO_2 necking phase. Connected TiO_2 domains were given the same color.

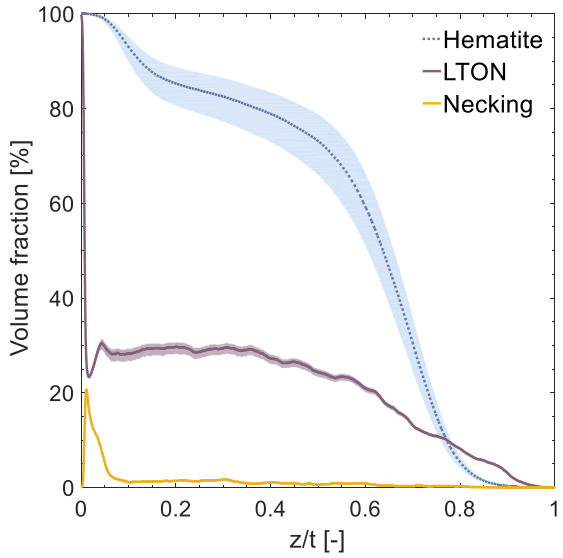

Figure S2: Volume fraction profiles through the normalized thickness of the photoelectrode films. The color shades around the hematite and LTON curves indicate the error bars assessed by an aggressive (Hematite: 150, LTON: 106) and conservative (Hematite: 100, LTON: 78) threshold-based segmentation. The hematite electrode with a maximum error bar of (+ 6%, - 8%) was more affected by segmentation uncertainty due to small 'cauliflower' branches with diameters below 30 nm, showing a strong edge effect (bright and blurry secondary electron signal from small features) in the SEM image. The outlines of the LTON particles have high contrast, i.e. a steep grey value gradient, and uncertainty in the pore segmentation lead to a maximum error bar of (+ 3%, -5%). The yellow curve shows the volume

fraction of the necking phase (TiO_2) in the LTON electrode only. The FTO substrate is located at z=0. The film thickness of the hematite sample is t=652 nm, and of the LTON sample is t=7.568 µm.

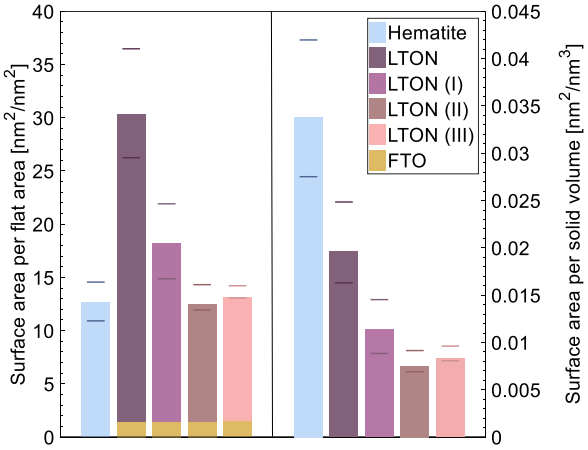

Figure S3: Surface area for hematite, LTON, LTON(I): LTON with only nano-pores connected to void space, LTON(II): LTON without nano-pores, LTON(III): LTON without nano-pores and without necking. Left: surface area per flat electrode area (*xy*-plane). Right: surface area per solid semiconductor volume. The error bounds indicate a lower bound segmentation threshold (hematite 100, LTON: 78) and an upper bound segmentation threshold (hematite 150, LTON: 106), to quantify the effect of the uncertainty in the segmentation process.

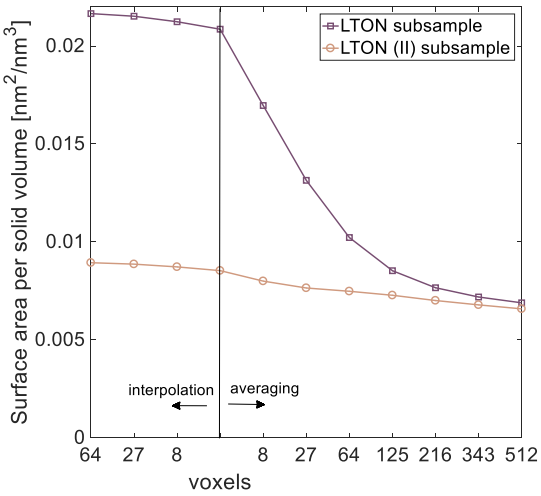

Figure S4: Mesh density study of surface area calculations. For subsamples (500 x 500 x 500 voxels) of the LTON and LTON(II), the surface area per solid volume are shown for different mesh densities. The coarsening of the mesh was achieved by averaging neighboring voxels, whereas the refinement was done by bicubic interpolation. The FIB-SEM resolution is shown to be sufficient to determine an accurate surface area for the LTON(II) (without nano-pores), as the surface area decreases only by 6% for an averaging of 8 voxels. The bicubic interpolation mainly represents a smoothing process of the mesh, and the deviation in the surface area stays within 5% for a refinement of 64 (4 x 4 x 4) per voxel. In case of the LTON with nano-pores, the calculations suggest that the FIB-SEM resolution is not high enough to prove surface mesh convergence. In the first averaging step, a decrease of the surface area by 19% is

observed. The limiting FIB-SEM resolution explains the smaller calculated surface area compared to the experimental BET measurement. The smoothing process has only a small effect on the final result by an increase of 4% for a refinement of 64.

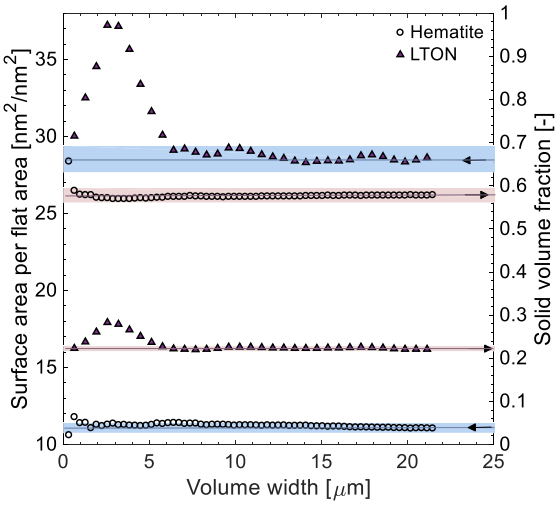

Figure S5: A representative volume (RV) is defined to be the smallest subvolume of the dataset for which the structural properties, surface and volume fraction, statistically represent the properties of the overall film. The solid volume fraction and the normalized surface area are computed on successively increasing subvolumes in order to determine the RV for the studied photoelectrodes. The volumes have a constant height and a fixed aspect ratio of the side lengths, corresponding to the aspect ratio of the full dataset. An initial volume with a depth of 160 nm and a width of 640 nm was defined in the center of the datasets. The volumes were considered representative when the average of the last 10 calculated values of solid volume fraction and the specific surface area, respectively, stayed within an error band of ± 3%.

The representative volume (RV) study was performed to analyze the homogeneity of the photoelectrodes and to draw conclusions about the minimum volume sizes which still represent the characteristics of the entire film, relevant also for subsequent transport calculations. The film roughness factor and the solid fraction are shown for increasing volume sizes (Figure S5). The aspect ratio of the volume width to the depth is kept constant at 4:1. For the hematite film, the size of the individual 'cauliflowers' is an order of magnitude smaller than the width and depth of the measured data set. A volume of 11.904 μm^3 (RV: width=8 µm, depth=2 µm) was required for film roughness and the solid volume fraction to stay within an error band of ± 3% for increasing volume sizes. The recorded volume of the hematite film is much bigger than the required representative volume. For the LTON electrode, a volume of 64.176 μm^3 (RV: width=5.73 µm, depth=1.4 µm) was required for film roughness and the solid volume fraction to stay within an error band of ± 3% for increasing volume sizes.

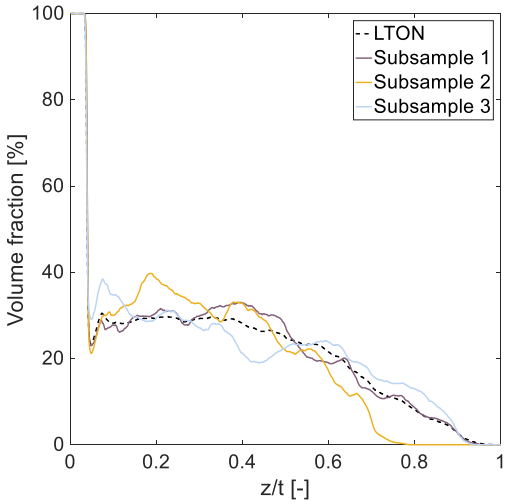

Figure S6: Subvolume for light absorption calculations and mass transport simulations. In order to address the variability of the film thickness in the LTON sample, a subsample with the volume of 8 RV was chosen. For the subsequent light absorption and transport calculations, the volume fraction distribution along the z-axis, the overall volume fraction as well as the surface area per flat area are crucial. Three subsamples (1000 x 1000 x 1000 voxels) were created and compared to the LTON sample. Subsample 1 represents the overall sample well and was chosen, with a mean absolute percentage deviation of 8% for the volume fraction distribution. The relative error of the overall volume fraction is 4% and the center of density is 19% lower. The surface area per flat surface is 10% higher. Subsample 2 has a lower film thickness, with a mean absolute percentage deviation of 35% for the volume fraction distribution. The relative error of the overall volume fraction is 1.7% and the center of density is 1.8% higher. The surface area per flat surface is 5% lower.

Subsample 3 has a mean absolute percentage deviation of 19% for the volume fraction distribution. The relative error of the overall volume fraction is 3% and the center of density is 5% higher. The surface area per flat surface is 2% higher.

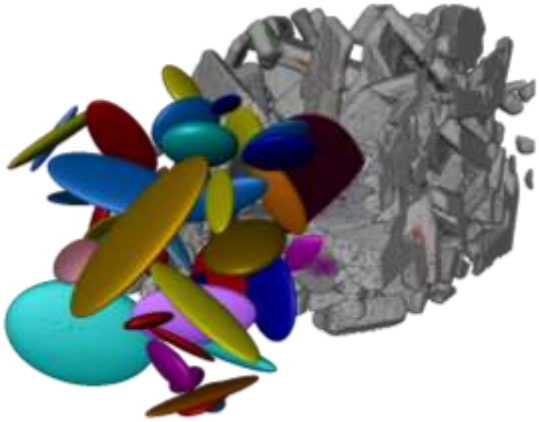

Figure S7: 3D rendering of ellipsoids fitted into the particles of the LTON photoelectrode.

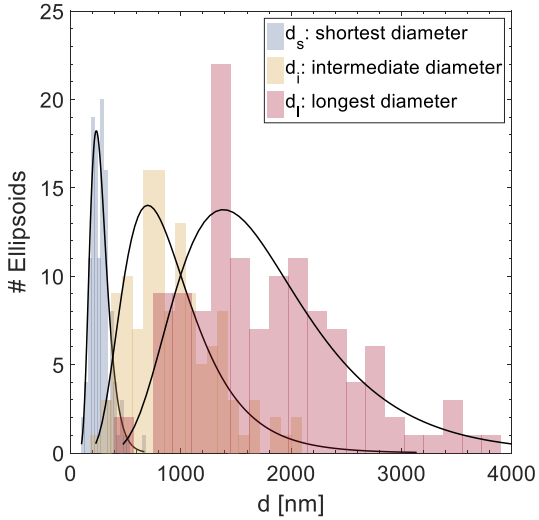

Figure S8: Size distribution of the three ellipsoid diameters with lognormal distributions: $d_{s,mean}$=272 nm, $d_{s,SD}$=88 nm; $d_{i,mean}$=932 nm, $d_{i,SD}$=427 nm; $d_{l,mean}$=1789 nm, $d_{l,SD}$=773 nm.

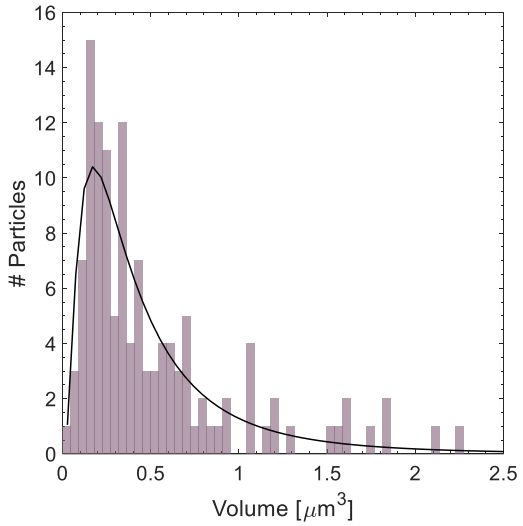

Figure S9: Particle volume distribution (volumes of the smallest box in which the ellipsoid fits). Lognormal distribution: mean =0.521 µm^3, SD=0.544 µm^3, median=0.338 µm^3.

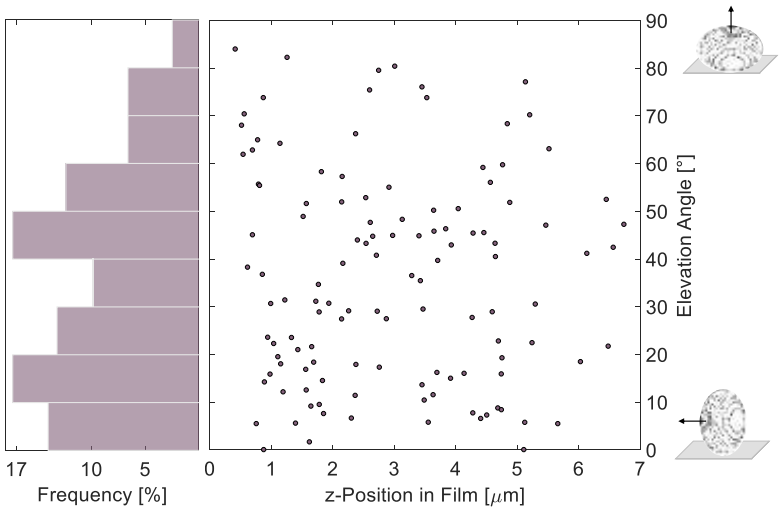

Figure S10: Particle orientation determined by the direction of the smallest diameter. Elevation angle=90°: particle lies flat relative to the FTO, and elevation angle=0°: particle stands upright relative to the FTO. The scatter plot demonstrates no trend of particle orientation as a function of z-position; however, normal vectors of the particles were elevated most frequently by 10° or 45°, as shown in the frequency distribution.

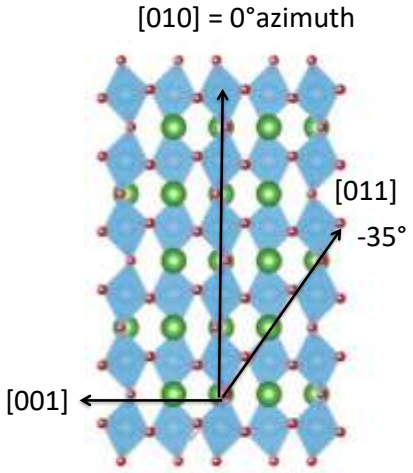

Figure S11: Projection of a typically-shaped monocrystalline LTON particle in [100] direction consisting of three unit cells in [001], two unit cells in [010] and two unit cells in [001] direction. Green spheres indicate the La positions, blue spheres the O positions and orange spheres the N positions; the red spheres in the center of the octahedral coordination polyhedron are Ti atom. O and N share unit cell positions. The pore elongation direction [011] is shown. The image was generated using the Vesta code (K. Momma, and F. Izumi: Vesta 3 for Three-Dimensional Visualization of Crystal, Volumetric and Morphology Data. J. Appl. Crystallogr. 44, 1272 (2011).

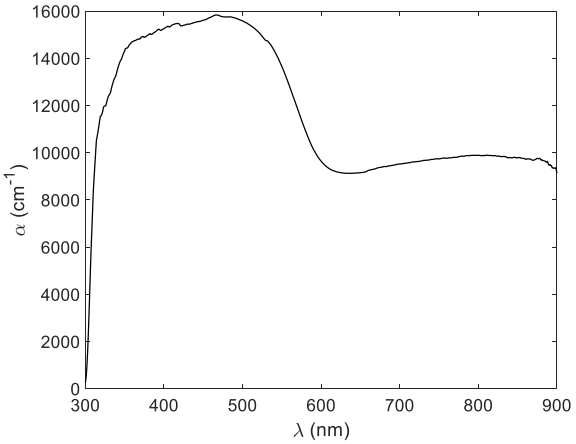

Figure S12: Absorption coefficient as a function of the wavelength. The bandgap of LTON is 2.1 eV and corresponds to 590 nm. The wavelength-averaged value of α between 300 nm and 590 nm is $1.4 \cdot 10^4$ cm^{-1}.

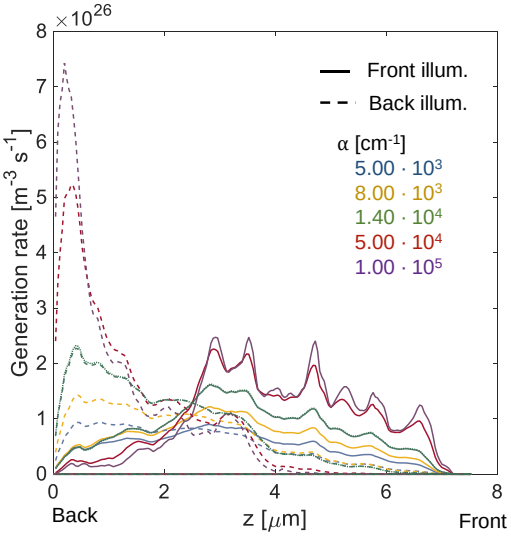

Figure S13: Calculated generation rates for front and back illuminations integrated over all the discretized columns in x- and y-direction. The generation rates for the measured, wavelength-dependent absorption coefficient is shown in a green dotted line for front and back illumination. The mean deviation from the exact profile to a constant, wavelength-averaged absorption coefficient of $1.4 \cdot 10^4$ cm^{-1} is 1.1% and 1.6% for front and back illumination, respectively. The profiles for an additional 4 constant absorption coefficients are shown.

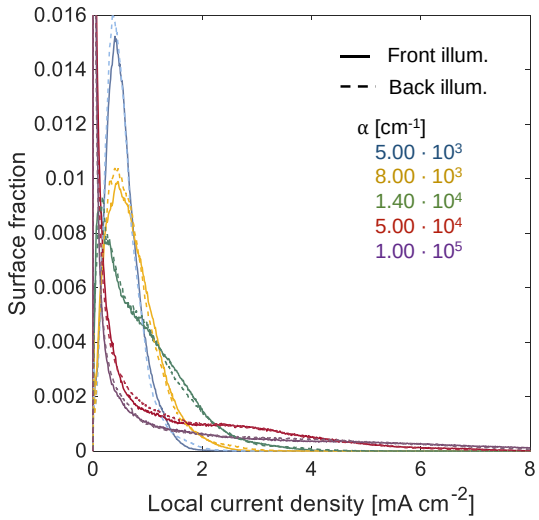

Figure S14: Local current density distribution for front and back illumination with constant, wavelength-dependent absorption coefficients.

$5.00 \cdot 10^3$ [cm^{-1}]
Front illum.: peak @ 0.4, max @ 2.38 [mA cm^{-2}] ; Back illum.: peak @ 0.36, max @ 2.72 [mA cm^{-2}]
$8.00 \cdot 10^3$ [cm^{-1}]
Front illum.: peak @ 0.45, max @ 3.16 [mA cm^{-2}] ; Back illum.: peak @ 0.4, max @ 3.66 [mA cm^{-2}]
$1.40 \cdot 10^4$ [cm^{-1}]
Front illum.: peak @ 0.12, max @ 4.31 [mA cm^{-2}] ; Back illum.: peak @ 0.17, max @ 4.99 [mA cm^{-2}]
$5.00 \cdot 10^4$ [cm^{-1}]
Front illum.: peak @ 0.01, max @ 7.98 [mA cm^{-2}] ; Back illum.: peak @ 0.01, max @ 8.86 [mA cm^{-2}]
$1.00 \cdot 10^5$ [cm^{-1}]
Front illum.: peak @ 0.0.1, max @ 9.86 [mA cm^{-2}] ; Back illum.: peak @ 0.01, max @ 10.77 [mA cm^{-2}]

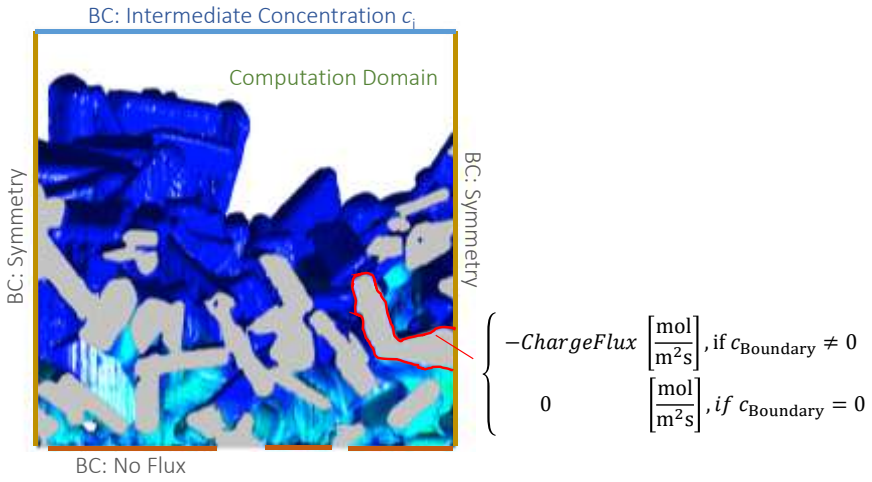

Figure S15: An intermediate concentration ci was set as a top boundary condition. The side walls had symmetry boundary conditions and the bottom, which was covered by FTO had a no-flux boundary condition. The calculated local current density was applied as a reactant sink boundary condition onto the electrolyte-semiconductor interface.

The boundary flux was given as a step function, being the charge flux calculated by the generation rate for a boundary concentration $c_{Boundary} > 0$, and being 0 for $c_{Boundary} = 0$.

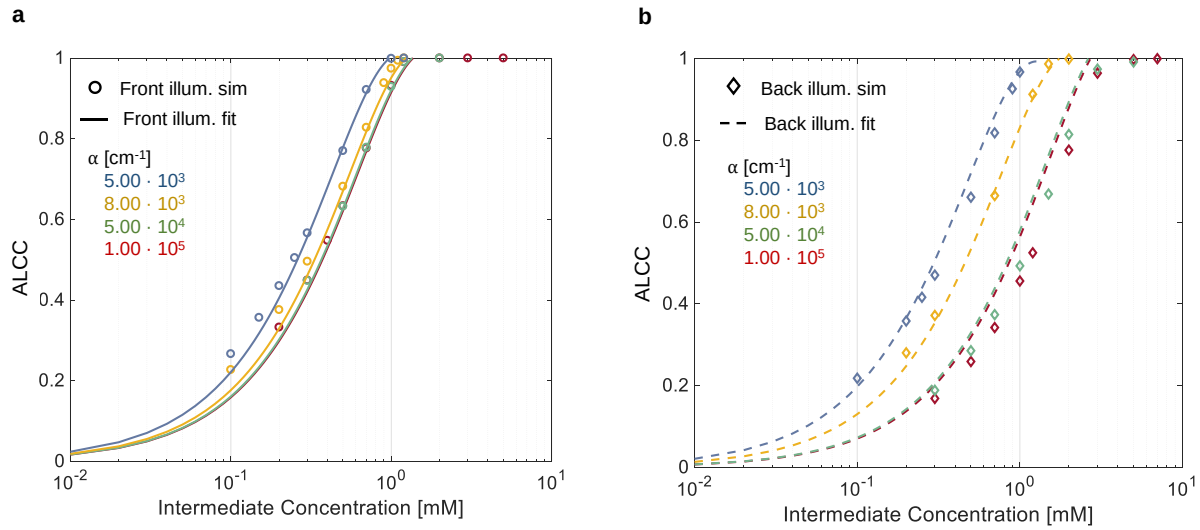

Figure S16: Simulation values and fit of *ALCC* vs intermediate concentration for different, wavelength-averaged absorption coefficients: (a) front illumination and (b) back illumination. For increasing absorption coefficients, the curves merge asymptotically, as the generation rate profile, and therefore the *ALCC,* is only dependent on the morphology.

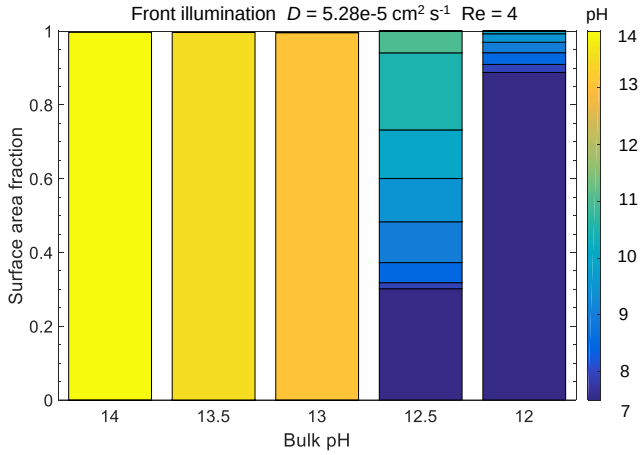

Figure S17: Surface fraction of local surface concentrations for a given bulk pH in a flow cell water splitting device with NaOH as an electrolyte and a flow regime of *Re*=4.

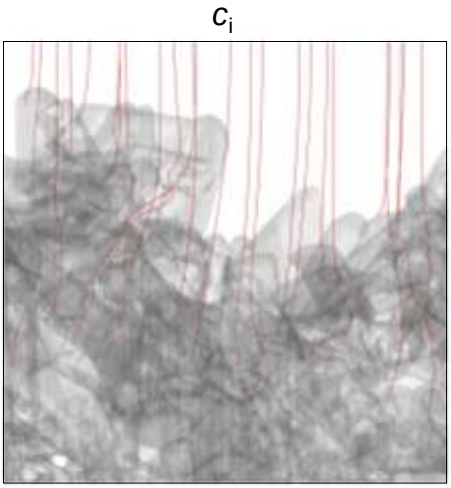

Figure S18: Visualization of 25 random reactant paths for front illumination, $D=5.28\cdot10^{-5}$ $cm^2\ s^{-1}$, and $\alpha=1.4\cdot10^4$ cm^{-1}.

[Animation_SA_LTONwithTiO2.mpg]

Animation SA: Animation of LTON photoelectrode with the TiO_2 necking phase. Connected TiO_2 domains were given the same color.

[Animation_SB_EllipsoidInLTON.mpg]

Animation SB: Animation of ellipsoids fitted into the particles of the LTON photoelectrode.

[Animation_SC_PoreOrientation.mpg]

Animation SC: Animation of an ellipsoid (blue) fitted into a LTON particle, and of the nano-pores within the ellipsoid.

[Animation_SD_TEM_Tomography.mp4]

Animation SD: STEM Tomography animation through a LTON-particle oriented roughly in [100] orientation showing the complex porous network with a resolution of 7nm/pixel. The longest particle axis measures 2.2 µm. For electron tomography a JEOL single axis tomography holder was used. STEM/HAADF images were manually recorded at 2° tilt intervals over a range from −60° to 64°. The images were aligned using the StackReg plugin of the image processing software ImageJ. The 3D volume reconstruction was computed using 80 cycles of the simultaneous iterative reconstruction technique (SIRT) implemented in TomoJ, which is also an ImageJ plugin. Grey value histogram-based segmentation was applied. Finally, the 3D voxel projection and the orthoslices were generated with the Amira visualization program.